Available online at www.sciencedirect.com
ScienceDirect
Ceramics International 35 (2009) 1521–1527
CERAMICS INTERNATIONAL
www.elsevier.com/locate/ceramint

Characteristics impedance spectroscopy: Tool to characterize ion-blocking phenomena

Koushik Biswas *

Department of Metallurgical and Materials Engineering, Indian Institute of Technology, Kharagpur 721302, India

Received 18 April 2008; received in revised form 26 June 2008; accepted 20 August 2008
Available online 30 September 2008

Abstract

Scandia (Sc_2O_3) doped nano-crystalline zirconia powder was prepared by dissolution and co-precipitation method. Bulk specimens were prepared by sintering nano-powders at various temperatures. The characteristics admittance diagrams obtained from impedance spectroscopic measurement revealed the grain interior, defect (blocker) and grain boundary conductance. The ion-blocking model stressed the role played by the distribution of the current lines around the blockers and by the dielectric properties of these blockers. With temperature, no variation of the blocking factor was observed. This model is consistent as per similarity between the bulk and blocked conductance activation energies are concerned. The admittance diagram parameters were correlated to the geometrical parameters of the blockers.

Keywords: Nano zirconia; DTA; XRD; TEM; Impedance spectroscopy; Ion-blocking

1. Introduction

In solid ionic conductors, such as zirconia, ceria, thoria-based ionic conductors, beta (β)-Aluminas, NASICONs, etc., movement of ionic charge carriers can be hindered by blockers at internal interfaces. This blocking effect can also be observed in electronically conducting materials. The ion-blocking can be induced by various microstructural defects such as grain boundaries, cracks, pores and second phase inclusions [1–3]. The blocking phenomena are commonly observed in impedance spectroscopy and many researchers had used the ion-blocking model as tool to characterize these effects [3–16].

In materials with small and medium blocking magnitudes, the blocking effects appear approximately temperature-independent below a certain transition temperature. Above this temperature, the blocking effect gradually decreases and disappears [3,17]. Here, the critical parameter seems to be the electric conductivity of the conducting matrix and when conductivity exceeds value of over 0.001 S/cm, blocking effect becomes negligibly small [3]. Blocking effect is also effective only below a certain threshold frequency (f_1). To illustrate this behavior, consider Fig. 1(a), which shows an admittance diagram of dense sintered (specimen 8-SSZ-3) Scandia stabilized Zirconia (SSZ) at 400 °C. Below the characteristic frequency (f_1), the blocking due to grain boundary becomes effective and one can represent this by considering an additional equivalent circuit consists of resistance and capacitance (see Fig. 1(b)). Above this threshold frequency (f_1), all the blocking effect vanishes and the electrical behavior of a polycrystalline material will be same as that of single crystal of the same shape and size [3]. The conductance at this frequency can be considered as the single crystal conductance or the bulk conductance (Σ_{bulk}). The general reduction in conduction from f_1 (Σ_{bulk}) to dc condition (Σ_{dc}) is generally attributed to trapping of a certain fraction of mobile charge carriers [3]. This phenomenon can be considered as blocking of certain fraction of oxygen (anionic) vacancies in the material by the blocker below the threshold frequency limit of f_1.

Quantitatively, the ion-blocking can be characterized by defining a blocking factor α_R as [17]:

$$\alpha_R = \frac{\Sigma_{bulk} - \Sigma_{dc}}{\Sigma_{bulk}} = \frac{\Sigma_{bd}}{\Sigma_{bulk}} \quad (1)$$

where Σ_{bd} is the blocked conductance that describes the blocking effect with the parallel equivalent circuit shown in Fig. 2. The representation of such an equivalent circuit truly

* Tel.: +91 3222 283244; fax: +91 3222 282280.
E-mail address: k_biswas@metal.iitkgp.ernet.in.

0272-8842/$34.00
doi:10.1016/j.ceramint.2008.08.013

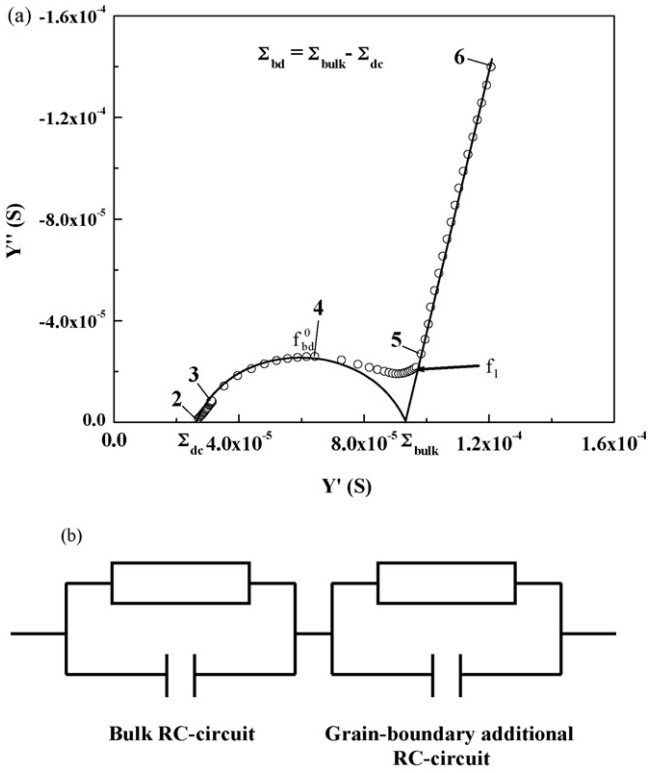

Fig. 1. (a) Admittance diagram of 8-SSZ-3 specimen at 400 °C showing the bulk, dc and the blocked conductances. The numbers indicate the logarithm of measuring frequencies. (b) The equivalent circuit diagram representing bulk and grain boundary contributions.

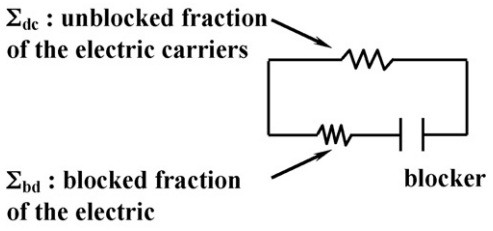

Fig. 2. Equivalent parallel circuit describing the ion-blocking effect [3].

related to specific properties of the blocker and can be deduced from the admittance diagrams. Several researchers [1–3,7,17] showed that the blocked conductance extracted from the admittance plot varies with the temperature and in most cases, very similar to the bulk conductance. This indicates that identical electric (or charge) carriers are responsible for the bulk and block conductance.

In the present investigation, parameters associated with blocking effects are extracted from the admittance diagrams using ion-blocking model and impedance spectroscopy technique and these parameters are correlated with the dimensions of the blockers estimated from the microstructural observations.

2. Experimental

Commercially available $ZrOCl_2{\cdot}8H_2O$ (purity 99.95%, STERM Chemicals, USA) and Sc_2O_3 (99.9% (Sc), STERM chemicals, USA) powders were used as starting materials to synthesize 8 mol.% Scandia stabilized Zirconia (8-SSZ). Two precursor solutions were prepared by dissolving $ZrOCl_2{\cdot}8H_2O$ in distilled water and Sc_2O_3 in hot concentrated HCl. Precursor solutions were then mixed and stirred continuously to obtain a homogeneous solution. Co-precipitation was done by adding 5% NH_4OH solution as hydrolyzing agent to the precursor solution keeping pH within 9–10. The formula mass ratio was determined by weighing the resulting oxides mass obtained after calcinations of a known amount of precursor. The precipitates were rinsed thoroughly and dried overnight. The resulting powders were then calcined at 900 °C for 2 h in air. After calcinations, the powders were ground and compacted at 250 MPa to obtain the green pellets. Sintering was carried out in a tubular resistance furnace between the temperature range of 1100–1400 °C for 0.5, 1 and 2 h in air with a heating and cooling rate of 10 °C/min.

Thermal stability and the phase transformation of the resultant powder were studied using a differential thermal analyzer (PERKIN ELMER INSTRUMENTS, USA) over a temperature range from room temperature to 1300 °C at a heating and cooling rate of 20 °C/min.

The density of the sintered pellets was measured by Archimedes' water displacement principle:

$$\rho_s = \frac{m_s \rho_s}{m_s - m_w} \tag{2}$$

where ρ_s and ρ_w are the sintered and water density, respectively. m_s and m_w are the mass of the sintered pellet and mass of the pellets in the water, respectively. The relative density (ρ_{rel}) was calculated by dividing the sintered density (ρ_s) by the theoretical density (ρ_{th}) calculated from the rule of mixtures.

Microstructures of the calcined powder and sintered specimens were examined with scanning electron microscope (JEOL, Japan) and transmission electron microscope (CM-12, Philips, Holland). The qualitative phase analysis was done by X-ray Diffraction (PW 1840 diffractometer control, Phillips, Holland) using filtered Cu Kα radiation with a wavelength of λ = 1.54 Å and then by comparing the X-ray diffraction patterns with the JCPDS standards. The calcined and sintered specimens were ground to fine powders in order to avoid any texturing effects. The powder particle size (D) was also estimated from XRD plots using the Debye Scherrer's formula:

$$D = \frac{0.94\lambda}{\cos\theta_B (B^2 - b^2)^{1/2}} \tag{3}$$

where λ is the wavelength of the characteristic X-ray, B and b are the full-width at half-maximum of the corresponding XRD peak of strain free and sintered/calcined sample, respectively.

For electrical characterization, the sample pellets were contacted by sputtering of a ~50 nm Pt layer followed by coating with platinum paste and heat-treated at 800 °C for 1 h to burn out the binder of the platinum paste. AC impedance measurement is performed using HIOKI 3532 LCR, HiTester, JAPAN, in the temperature range 50–500 °C over a frequency range from 100 Hz to 1 MHz.

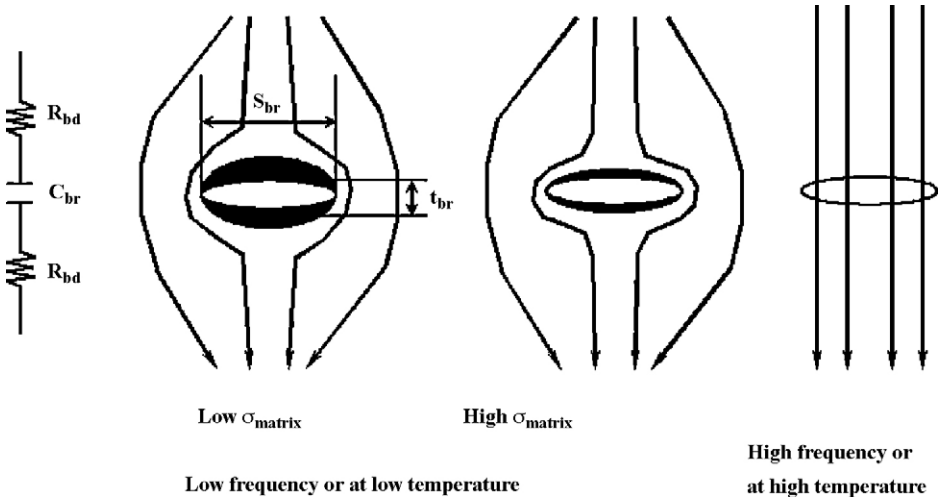

Fig. 3. Model showing the isolated spaces on both side of the blocker. Increase in matrix conductivity results in smaller isolated spaces. At high frequency or temperature, the blocking effect vanishes [3]. C_{br}, R_{bd}, S_{br} and t_{br} are the blocker capacitance, resistance, blocker area normal to the electric field and equivalent thickness, respectively.

3. Ion-blocking model

The model used in the present study is very similar to that of used by Kleitz, Dessemond and their co-workers [3,17]. However the modified estimation process in our study makes it more reliable than the old conventional models. The novelty in present work comes from the approach that bulk defects can be estimated from the characteristics Debye length (L_D) and the dc conductivity (Σ_{dc}) and not relying on the basis of microstructural examination which often associated with manual errors (statistical). Thus our modified process will certainly provide better accuracy compared with previous studies. The schematic representation of blocker's dimensions is shown in Fig. 3. The distribution of current lines around the blocker forms an isolated zone, which diminishes with increase in higher matrix conductivity or increase in temperature/frequency.

This model is based on the following assumption made by several researchers [3,11,17]:

- the equivalent blocked conductance only represents the behaviour of blocked electric carriers and hence it is proportional to the specific conductivity of the material, i.e.,

$$\Sigma_{bd} = k_{bd}\sigma_{bulk} \tag{4}$$

  where k_{bd} is an appropriate geometrical factor.
- the capacitive behavior of the blocking effect (C_{br}) is predominantly govern by the dielectric response of the blocker, which in turn related to the geometrical factor of the blocker (in simple case, related to blocker area normal to the electric field (S_{br}) and corresponding equivalent thickness (t_{br}) (Fig. 3)), i.e.,

$$C_{br} = \frac{\varepsilon_{br}\varepsilon^0}{k_{br}} = \frac{\varepsilon_{br}\varepsilon^0 S_{br}}{t_{br}} \tag{5}$$

  where ε_{br} is the blocker dielectric constant.
- capacitive behavior is dominated by the space-charge in the conducting phase.

In order to estimate the blocker size, Dessemond and co-workers [17] defined a frequency factor (α_F) which is given by:

$$\alpha_F = \frac{f^0_{bd}}{f^0_{bulk}} \tag{6}$$

where f^0_{bd} and f^0_{bulk} are blocked and bulk semicircle (in impedance/admittance diagram) relaxation frequencies.

For blocking process, the relaxation equation is given as:

$$\frac{2\pi f^0_{bd} C_{br}}{\Sigma_{bd}} = 1 \tag{7}$$

and that of bulk is:

$$\frac{2\pi f^0_{bulk}\varepsilon_{bulk}\varepsilon^0}{\sigma_{bulk}} = 1 \tag{8}$$

Combining the previous equations, the frequency factor can be expressed in terms of blocker dimensions:

$$\alpha_F = \frac{f^0_{bd}}{f^0_{bulk}} = \left(\varepsilon_{bulk}\frac{k_{bd}}{S_{br}}\right)\frac{t_{br}}{\varepsilon_{br}} \tag{9}$$

Considering the blocked spaces are typically charged regions, the geometrical factor k_{bd} is given as [3]:

$$k_{bd} \approx 2S_{br}L_D \tag{10}$$

where L_D is the Debye length of the bulk material.

The Debye length can be estimated from the following equation [18]:

$$L_D = \left(\frac{\varepsilon_{bulk}\varepsilon^0 k}{Tq^2N}\right)^{1/2} \tag{11}$$

where k and q are Boltzmann's constant and elemental charge, respectively. N is the concentration of the bulk majority carriers at temperature T and is usually related to the dc conductivity of the material by [19]

$$\sigma_{DC} = \left(\frac{Nq^2d^2\gamma}{6}\right)\left(\frac{f_p}{kT}\right) \quad (12)$$

where $d^2\gamma$ (= $0.35a^2$) is related to the lattice parameter a, f_p is characteristics hopping frequency.

4. Results and discussions

Differential Thermal Gravimetric (DTG) curve (Fig. 4) of the resultant powder shows two exothermic peaks in the temperature range of 200–400 °C along with a small peak near 500 °C. These peaks indicate that most of the volatile substances (e.g., Cl_2, NO_2, NH_4) eliminated in this temperature region. Above 800 °C there was no mass loss in powder, indicating that, stabilized zirconia will be formed above this temperature. During cooling no phase transformation takes place indicating the stability of the 8 mol.% scandia stabilized zirconia [20].

The transmission electron microscope (TEM) image of the 8-SSZ nano-particles, shown in Fig. 5, reveals that the particles are highly crystalline, have a uniform size distribution and a mean measured particle size of ~42 nm. The selected area diffraction pattern (inset) corroborates the existence of a nano-crystalline powder. Fig. 6 shows the XRD patterns obtained from the calcined and sintered specimen. In the 8-SSZ specimen, all peaks could be assigned on the basis of a cubic and tetragonal structure. As the tetragonal ($P4_2/nmc$) phase is slightly distorted from the cubic phase ($Fm\bar{3}m$) and peaks are broadened due to the nano-particle size, it is very difficult to differentiate between these two crystal phases using the X-ray diffraction pattern. However, several authors have reported the presence of both tetragonal and cubic phases [21,22]. The phase diagram in the ZrO_2–Sc_2O_3 system [23] predicts the existence of a monoclinic phase if the specimen is cooled to equilibrium conditions. However, the 8-SSZ specimen processed under similar conditions does not show the presence of the monoclinic phase.

Densities of the sintered specimens are tabulated in Table 1. The average crystallite and the grain sizes for calcined and sintered samples are determined using Scherrer's formula (Eq. (1)) and are also tabulated in Table 1.

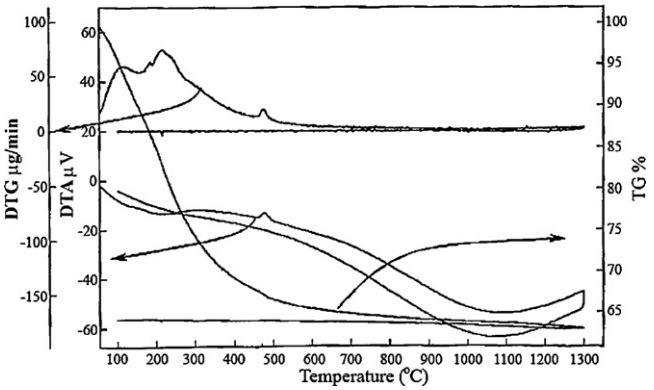

Fig. 4. Thermo-gravimetric analysis of precursor derived co-precipitated 8-SSZ powder from room temperature to 1300 °C.

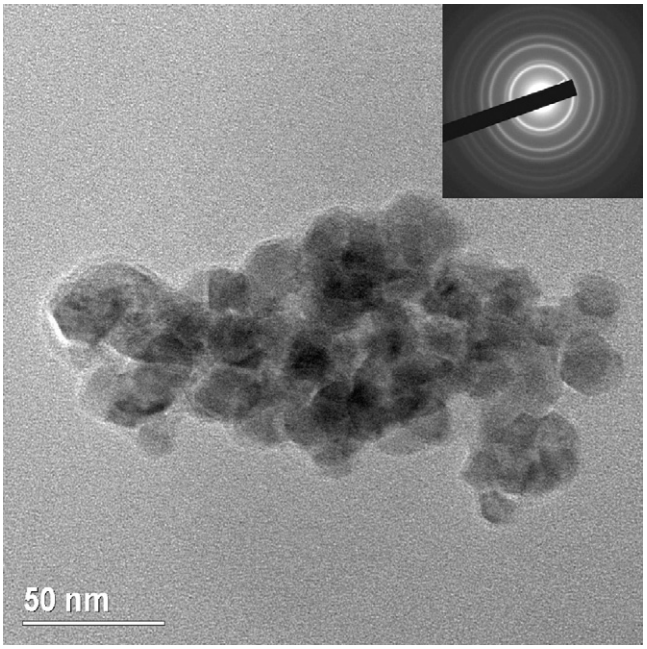

Fig. 5. Transmission electron micrograph of 8-SSZ nano-crystalline powder calcined at 900 °C for 2 h, showing the selected area diffraction (SAD) pattern (inset).

Scanning electron micrographs (SEM) of dense and porous sintered specimens are shown in Fig. 7(a) and (b), respectively. Dense nano-sized faceted grains are observed in case of the specimens sintered at elevated temperatures (above 1350 °C). The densification and the average particle size increase with increase in sintering temperature and time. Sluggish rate of densification (due to slow diffusion of the chemical species at lower temperature) at lower temperatures leads to formation of porous microstructure.

Fig. 8 represents a typical admittance diagram obtained from a porous (87% dense) 8-SSZ-8 specimen. The circular fitting of

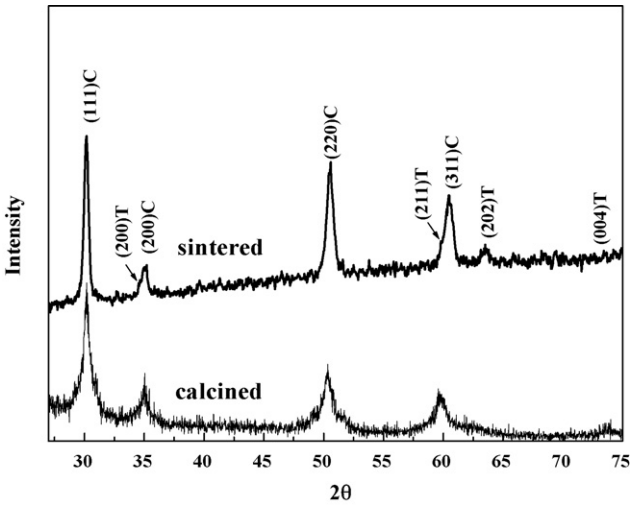

Fig. 6. X-ray diffraction pattern of 8-SSZ powder after calcination at 900 °C for 2 h followed by sintering at 1400 °C for 2 h.

Table 1
Densification behavior and particle/grain size analyses of calcined and sintered specimens.

Powder/sample denomination	Processing condition			% Theoretical density	Average particle/grain size (nm)	
	Calcination (900 °C; 2 h)	Sintering			XRD	SEM/TEM
		Temperature (°C)	Time (h)			
8-SSZ	✓	×		–	38.5 ± 4.3	~42
8-SSZ-1	✓	1400	0.5	98.7	312 ± 15.3	~325
8-SSZ-2	✓	1400	1.0	98.9	323 ± 16.1	~335
8-SSZ-3	✓	1400	2.0	99.3	337 ± 15.2	~350
8-SSZ-4	✓	1350	1.0	98.1	311.7 ± 14.1	~330
8-SSZ-5	✓	1350	2.0	98.8	322.7 ± 16.2	~330
8-SSZ-6	✓	1200	2.0	91.2	290 ± 11.3	~310
8-SSZ-7	✓	1100	0.5	83.6	271 ± 12.4	~300
8-SSZ-8	✓	1100	2.0	87.2	279 ± 13.5	~300

the complex admittance plot by using the program EQ developed by Boukamp [24,25] yields different conductance contributions. The low frequency semicircle is attributed to the grain boundary blocking whereas the high frequency curve is the characteristic response obtained from the pore structure.

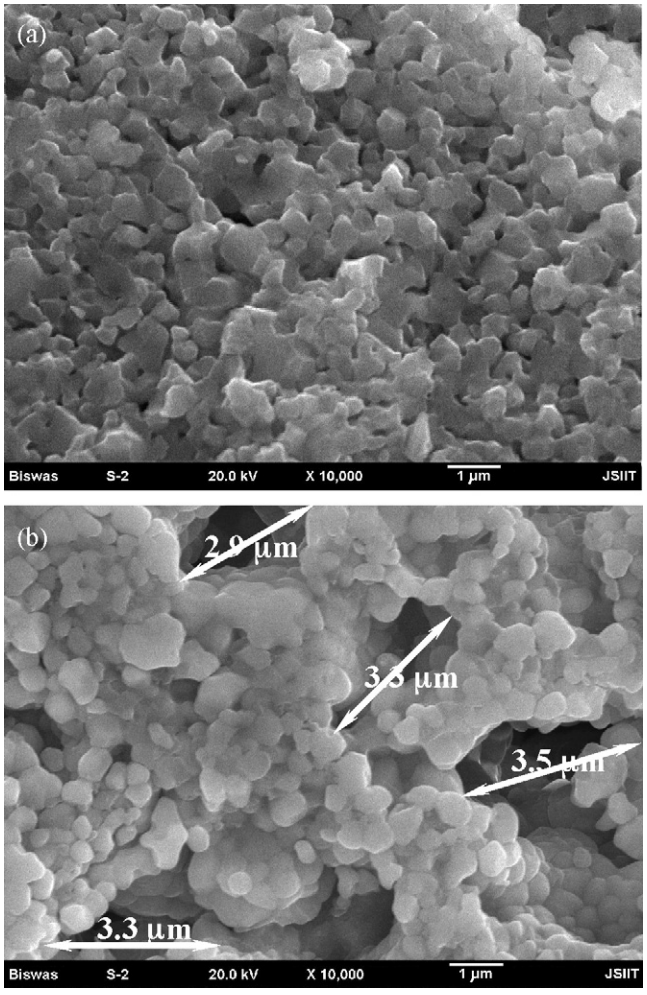

Fig. 7. Scanning electron micrographs of bulk fracture surfaces showing the nano-grain structure of (a) 8-SSZ-3 and (b) 8-SSZ-8 specimens. Sample 8-SSZ-8 shows the porosity of comparable dimensions as found using ion-blocking model.

The blocking factor (α_R) and the frequency factor (α_F) are calculated using Eqs. (1) and (6), and are plotted in Fig. 9. Both these factors are approximately constant over the measured temperature range. It is worth mentioning that, the model represented here is mostly applied under constant α_R conditions, for which the experimental data is much simpler to interpret. The value obtained in the present investigation follows the applicability criteria of this model very well.

The temperature dependence of the conductivity shows an Arrhenius type of behaviour and can be represented as:

$$\sigma = \sigma_0 \exp\left(-\frac{E_a}{kT}\right) \tag{13}$$

where σ_0 is the pre-exponential factor which depends on structural parameters and the number of charge carriers, E_a is the activation energy for the conduction.

The bulk and the blocked conductances, deduced from the admittance diagram, behave similarly with temperatures (see Fig. 10) indicating that identical electric carriers are responsible

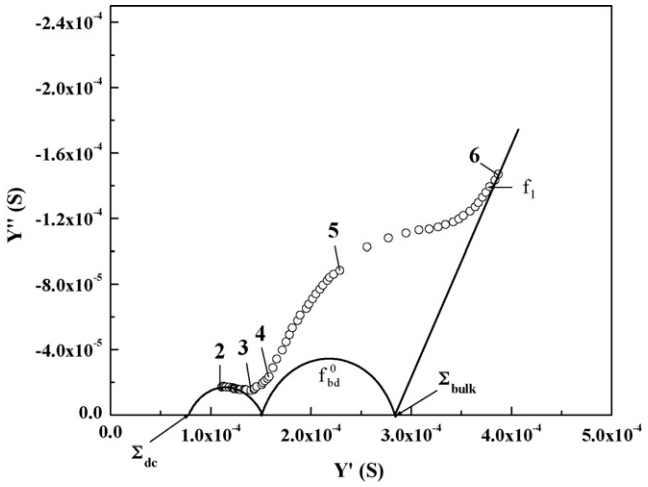

Fig. 8. Admittance diagram of 8-SSZ-8 sample at 450 °C. The low frequency semicircle is attributed to the grain boundary response and the high frequency semicircle is that of the pores. The pore characteristic semicircle is relaxing at ~10^5 Hz. The numbers indicate the logarithm of measuring frequencies.

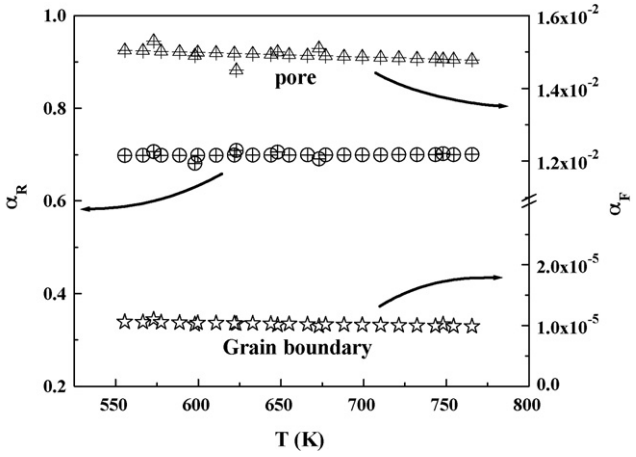

Fig. 9. Variation of blocking factor with the temperature. The characteristics frequency factor for grain boundary and pore are also showed as a function of temperature.

for these two physical parameters. Kleitz et al. [3] also observed a similar type of behavior. The activation energies associated with bulk and blocked conduction are indicated in Fig. 10.

In the previous study [26], characteristics hopping frequencies and dc conductivities are estimated from the impedance plots. The bulk charge carrier concentration (N) is estimated using Eq. (12) and former values and found to the in the order of 2.1×10^{22} m^{-3}. Substituting N in Eq. (11), the characteristic Debye length (L_D) is calculated to be ~51 nm at 400 °C. Using calculated L_D and Eqs. (9) and (10), the following numerical expression is obtained for characteristics blocker dimensions:

$$t_{br} = 9.804\alpha_F\varepsilon_{br} \quad (14)$$

The numerical factor calculated here is quite close (deviation < 10%) to calibrated value obtained by other researchers [3]. Using $\varepsilon_{br} = 23.9$ (this approximation is not unreasonable in view of the fact that the dielectric constant of

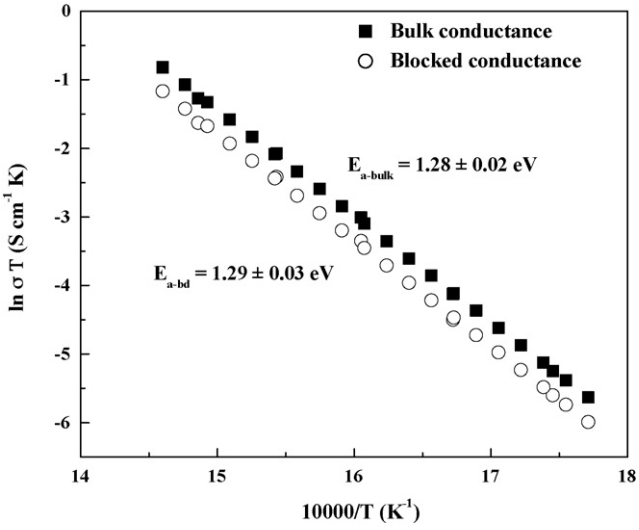

Fig. 10. Arrhenius diagram of bulk and block conductances showing activation energies for these processes. Similar behavior with respect to temperature indicates identical carriers for these two parameters.

ZrO_2 is quite composition insensitive [27,28]) and $\alpha_F \cong 10^{-5}$ (see Fig. 9) in Eq. (14), the average thickness of the grain boundary blockers is estimated to be ~2.34 nm. Although the value obtained is lower than the value found for zirconia stabilized with yttria dopants [28–33], it seems to be realistic considering the error associated with calculations and assumptions. Moreover, doping with almost similar size cation ($r_{Sc^{3+}} = 87$ pm, $r_{Zr^{4+}} = 84$ pm) may cause reduced segregation effect resulting lower grain boundary thickness [34].

In case of porous 8-SSZ-8 specimen, the frequency factor calculated from the pore relaxation semicircle (shown in Fig. 8) is found to be 0.015 (see Fig. 9) and hence the average blocker (pores/voids) dimension is estimated to be 3.5 μm. Microscopic examination (Fig. 7(b)) reveals that the blocker dimension agree reasonably well with the calculated value.

5. Conclusions

Uniform sized Scandia stabilized Zirconia powders were successfully synthesized using a co-precipitation method. Dense nano-crystalline stabilized zirconia was fabricated above 1350 °C. The characteristic impedance spectroscopic response clearly separates the bulk and block conductances. Geometric parameters of the blockers can be determined from the characteristic admittance plots of blocking processes. Despite variations in calculated parameters, the ion-blocking model could be used as a tool to measure the blocker dimensions within the realistic limits. Extrinsic defects dimensions determined using this model was found to reasonably match microscopic examination measurements.

Acknowledgments

The author extends his thanks to Laboratory assistants of Department of Metallurgical and Materials Engineering for their extended help in characterizing the specimens. He is also thankful to Professor D.-Y. Kim for providing facilities needed for synthesis and characterization, useful discussions and support during his stay at Seoul National University, South Korea. He would also like to thank the group members of Sintering and Microstructure laboratory, Creative Research Centre, School of Materials Research Centre, School of Material Science, and SNU, South Korea.

References

[1] M. Kleitz, C. Pescher, L. Dessemond, in: S.P.S. Badwal, M.J. Bannister, R.H.J. Hannink (Eds.), Science and Technology of Zirconia V, Technomic Publishing Company, Lancaster, PA, USA, 1993, p. 593.
[2] M.C. Steil, F. Thevenot, L. Dessemond, M. Kleitz, in: P. Duran, J.F. Femandez (Eds.), Third Euro Ceramics, Vol. 2, Properties of Ceramics, Faenza Editrice Ibbrica, San Vincente, Spain, 1993, p. 271.
[3] M. Kleitz, L. Dessemond, M.C. Steil, Solid State Ionics 75 (1995) 107.
[4] M.V. Inozemtsev, M.V. Perfil'ev, A.S. Lipilin, Elektrokhimiya 10 (1471) (1974) 1471.
[5] N.M. Beekmans, L. Heyne, Electrochim. Acta 21 (1976) 303.
[6] D.Y. Wang, A.S. Nowick, J. Solid State Chem. 35 (1980) 325.

[7] M. Kleitz, H. Bernard, E. Femandez, E. Schouler, in: A.H. Heuer, L.W. Hobbs (Eds.), Advances in Ceramics, Vol.3, Science and Technology of Zirconia, The Am. Ceram. Soc., Washington, DC, 1981, p. 310.
[8] M.J. Verkerk, B.J. Middelhuis, Solid State Ionics 6 (1982) 159.
[9] S.P.S. Badwal, J. Mater. Sci. 19 (1984) 1767.
[10] N. Bonanos, R.K. Slotwinski, B.C.H. Steele, E.P. Butler, J. Mater. Sci. 19 (1984) 785.
[11] J. Maier, Ber. Bunsenges. Phys. Chem. 90 (1986) 26.
[12] S.P.S. Badwal, J. Drennan, J. Mater. Sci. 22 (1987) 3231.
[13] B.C.H. Steele, in: T. Takahashi (Ed.), High Conductivity Solid Ionic Conductors, World Scientific, Singapore, 1989, p. 402.
[14] S.P.S. Badwal, Appl. Phys. A 50 (1990) 449.
[15] S.P.S. Badwal, J. Drennan, A.E. Hughes, in: J. Nowotny (Ed.), Science of Ceramic Interfaces, Elsevier, Amsterdam, 1991, p. 227.
[16] U. Lauer, J. Maier, J. Electrochem. Soc. 139 (1472) (1992) 1472.
[17] L. Dessemond, R. Muccillo, M. Henault, M. Kleitz, Appl. Phys. A 53 (1993) 57.
[18] H.L. Tuller, Solid State Ionics 131 (2000) 143.
[19] J.A. Kilner, B.C.H. Steele, in: O.T. Sorensen (Ed.), Nonstoichiometric Oxides, Academic Press, New York, 1981, p. 237.
[20] F. Boulc'h, E. Djurado, Solid State Ionics 157 (2003) 335.
[21] O. Yamamoto, Y. Arati, Y. Takeda, N. Imanishi, Y. Mizutani, M. Kawai, Y. Nakamura, Solid State Ionics 79 (1995) 137.
[22] M. Hirano, S. Watanabe, E. Kato, Y. Mizutani, M. Kawai, Y. Nakamura, Solid State Ionics 111 (1998) 161.
[23] F.M. Spiridonov, L.N. Popova, R.Ya. Popilskii, J. Solid State Chem. 2 (1970) 430.
[24] B.A. Boukamp, Solid State Ionics 20 (1986) 301.
[25] B.A. Boukamp, Solid State Ionics 18–19 (1986) 136.
[26] K. Biswas, Communicated to Materials & Design (2007).
[27] M.C. Steil, F. Thevenot, M. Kleitz, J. Electrochem. Soc. 144 (1997) 390.
[28] X. Guo, J. Maier, J. Electrochem. Soc. 148 (2001) E121.
[29] X. Guo, W. Sigle, J. Fleig, J. Maier, Solid State Ionics 154–155 (2002) 555.
[30] J.-S. Lee, D.-Y. Kim, J. Mater. Res. 16 (2001) 2739.
[31] Y. Ikuhara, P. Thavorniti, T. Sakuma, Acta Mater. 45 (1997) 5275.
[32] S. Stemmer, J. Vleugels, O. van der Biest, J. Eur. Ceram. Soc. 18 (1998) 1565.
[33] M.J. Verkerk, B.J. Middelhuis, A.J. Burggraaf, Solid State Ionics 6 (1982) 159.
[34] X. Guo, Y. Ding, J. Electrochem. Soc. 151 (2004) J1.